ACS OMEGA

Article

Cite This: ACS Omega 2019, 4, 146−158

http://pubs.acs.org/journal/acsodf

Improved Corrosion Resistance of Steel in Ethanol Fuel Blend by Titania Nanoparticles and *Aganonerion polymorphum* Leaf Extract

Nguyen Si Hoai Vu,[†,‡,∥] Pham Van Hien,[‡,∥] Motilal Mathesh,[§] Vu Thi Hanh Thu,*[,†] and Nguyen Dang Nam*[,‡]

[†]Faculty of Physics and Engineering Physics, University of Science, VNU-HCM, 227 Nguyen Van Cu Street, District 5, Ho Chi Minh City 700000, Vietnam

[‡]Institute of Fundamental and Applied Sciences, Duy Tan University, 10C Tran Nhat Duat Street, District 1, Ho Chi Minh City 700000, Vietnam

[§]Systems Chemistry, Institute for Molecules and Materials, Radboud University, Heyendaalseweg 135, Nijmegen 6525 AJ, Netherlands

Supporting Information

ABSTRACT: A porous and low-density protective film on a steel surface in the corrosive environment can undergo deterioration even in the presence of organic inhibitors due to infiltration of aggressive ions into the pinholes and/or pores. This phenomenon is related to the localized corrosion that takes place even in the presence of an optimal concentration of organic corrosion inhibitors in the given medium. To overcome this issue, we have designed an organic protective film on a steel surface with the help of titania nanoparticles (TNPs) combined with an organic corrosion inhibitor derived from *Aganonerion polymorphum* leaf extract (APLE), all to be studied in a simulated ethanol fuel blend (SEFB). The TNPs with varied diameters and concentrations have been studied for examining their effect on the inhibition capacity of 1000 ppm APLE on the steel surface in SEFB medium using electrochemical and surface analysis techniques. Enhanced corrosion inhibition of the surficial film was observed in the presence of both the APLE inhibitor and small amounts of TNPs. A direct agreement was observed between the experimental and molecular dynamics theoretical investigations showcasing high binding energy between inhibitor molecules and steel substrates, resulting in a much higher adhesion of the protective film, good thermal stability of the adsorbent film, and electron abundance for the supply of steel substrate of inhibitor species.

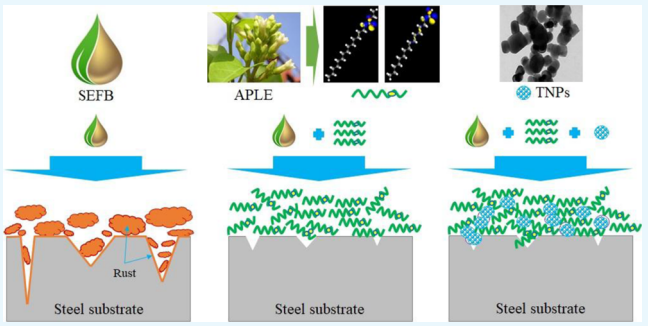

1. INTRODUCTION

The excessive use of fossil fuels, especially crude oil, leads to many negative effects on the environment and human health. The effects are not only limited to marine life and farmland but also extends to forest and air environment.[1−3] Therefore, it is the need of the hour to replace fossil fuels with renewable energies such as solar, wind, geothermal, tidal power, and biomass with biofuel as the most feasible solution.[4−6] Gasoline, the most widely used fuel for industrial and civil activities, is a liquid-type product of fossil fuels extracted through an oil refining process. Hence, it is also highly advisable to be partly or fully replaced by biofuel such as bioethanol. Unfortunately, due to technical and economic constraints, there is a very small window of opportunity for fully replacing gasoline by bioethanol. To overcome this, biogasoline, a mixture of traditional gasoline and bioethanol has emerged to be an optimal solution.[7] The volume percentage of bioethanol in biogasoline is marketed as E-grade, with E10 (10% ethanol) as the most popular biogasoline worldwide. Many governments have considered and adopted E85 because of its performance as well as affordable cost.[8−10] Despite many advantages of biogasoline, such as increasing engine combustion efficiency, lowering driving cost, decreasing particulate matter with sizes below 10 μm (PM10) that affects human health, reducing greenhouse gas emission, and minimizing emissions of SO_x and NO_x gas that, respectively, cause the global warming effect and acid rain, it does have a massive drawback, that is, the corrosion on fuel tanks and piping systems, which are mainly made of mild steel. The corrosion of steel could be caused by the hygroscopic properties of ethanol, aggressive contaminants in bioethanol, and bacteria in the blend.[11] To overcome this drawback, many manufacturers require supplement additives into biogasoline.[12−15] In recent years, the most widely used anticorrosive additives for gasoline are inhibitors including

Received: August 17, 2018
Accepted: December 7, 2018
Published: January 3, 2019

DOI: 10.1021/acsomega.8b02084
ACS Omega 2019, 4, 146−158

high-molecular-weight carboxylic acids, long-chain aliphatic amines, amine salts of carboxylic acids, and aliphatic polyamines and polyamides.[16] These inhibitors have shown poor pitting corrosion resistance and some of them even affect human health, but they are still widely being used owing to the lack of good and environmentally friendly inhibitors.[17] For the above reasons, it is necessary to look for alternative inhibitors for biogasoline that possess high-performance, ecological safety and easiness of manufacture, as well as high availability and economic viability. A new research trend on inhibitors using plant-extracted compounds has high potential in many corrosive environments such as H_2SO_4, HCl acidic conditions, chloride solutions, or biodiesel, and can be witnessed with the high number of publications.[18−21] Herein, for the first time, we have shown the potential application of leaf extracts from *Aganonerion polymorphum* as an effective corrosion inhibitor for steel in the biogasoline environment.

The above leaf extract was studied due to its popularity in South East Asian countries as a fresh vegetable with low-cost, as well as due to its environmental friendliness. Currently, there is a lack of research on exploring APL chemical composition, which would help in better understanding the nature of this leaf, as well as extending the scope for its application. Furthermore, there are very few reports on unconventional APL applications such as a green corrosion inhibitor for mild steel in an ethanol fuel blend. An earlier study[11] indicated that the extracting process could be simple and easy with inexpensive and nontoxic chemicals (ethanol and ethyl acetate). Additionally, the solvents can be collected and reused at the end of the process, which significantly reduces the cost of production. Particularly, APL's components could include natural derivatives such as aromatic amines and long hydrocarbon chain carboxylic acids and esters, which are in the commercial additive group for biogasoline and are also green in concept and efficient in cost. *A. polymorphum* leaf−ethyl acetate extract was investigated in the simulated ethanol fuel blend (SEFB) and was observed to inhibit steel corrosion.[11] The results indicated that APLE showed its best performance at 1000 ppm, and the inhibiting effect decreased with the increasing inhibitor concentration beyond 1000 ppm. The good corrosion performance was attributed to the protective film formation on the steel surface due to the adsorption of inhibitor species as an organic barrier layer. However, the main components that directly affected the corrosion inhibition of steel have not been examined yet. Furthermore, porosity including pores and pinholes is possible in the organic films, resulting in a lower film density on the substrate surface.[22] This could also result in delamination and localized corrosion through these pores and/or pinholes due to localized penetration and diffusion of the aggressive ions into the substrate forming a major cathode and a minor anode, leading to corrosion.[23] These are significantly related to localized corrosion even at an optimal concentration of the organic corrosion inhibitors. Overcoming these weaknesses of the organic inhibitors is very important to enhance its performance. Also, using theoretical methods such as molecular dynamics (MD) simulations and/or quantum mechanics techniques would provide insights and detailed understanding concerning electronic and molecular properties to unravel the adsorption of inhibitor molecules on active sites.

Nanoparticles have a large surface area, providing strong diffusion driving-force so that they can be assembled at the pores and/or pinholes in the organic film by their diffusion ability.[24,25] Among many types of nanoparticles, titanium dioxide nanoparticles (TNPs) is an outstanding material due to their chemical, thermal, and mechanical stabilities, as well as environmental friendliness and easiness of fabrication.[26] Their molecules have one atom of titanium and two atoms of oxygen with very high surface area which helps them to easily react with other molecules such as those comprising carbon atoms in the organic film,[27−29] suggesting them to be ideal candidates for self-healing the defects on the organic film to achieve a better barrier layer on the steel surface when organic inhibitors are adopted. Therefore, this study focused on the film formation process and mechanism of the protective layer on the steel surface when APLE was used in conjugation with TNPs as a green corrosion inhibitor, studied by experimental methods and molecular dynamics simulation. TNPs were used as synergistic inhibitors given their reinforcing ability in forming the protective layer on the steel surface. Particularly, the corrosion inhibition effect of APLE was studied using theoretical methods including density functional theory (DFT) and molecular dynamics (MD) simulations, which provided detailed electronic and molecular understandings regarding the adsorption of inhibitors on active sites under experimental conditions. DFT simulation provided information about inhibitor molecules that may affect its inhibiting properties, such as electro- or nucleophilic sites and orbital distribution. In addition, MD simulation also showcased the interaction between inhibitor molecules and the steel surface under different conditions such as temperature or pressure, including interaction energy, binding energy, and thermodynamics properties. The simulation process could serve as a platform for better understanding the interaction between the adsorbent materials and the substrate surface and providing a correlation with the experimental results.

2. RESULTS AND DISCUSSION

X-ray diffraction (XRD) was used to determine crystallinity and phase component of materials. For TNPs XRD pattern in Figure 1a, Joint Committee on Powder Diffraction Standards database was used to identify TiO_2 crystalline peaks of anatase, brookite, and rutile phases (card nos. 21-1272, 29-1360, and 21-1276). As seen in Figure 1a, there are three anatase peaks (A), no brookite peak (B), and four rutile peaks (R) with the relatively high intensity of the R(210) peak. Peak search parameters of the XRD pattern were analyzed by PANalytical X'Pert Highscore Plus version 3.0.0. On the basis of the analyzed results, the TNPs average crystalline size was determined by the Scherrer equation. The calculated average sizes and weight fraction of TNPs related to Figure 1a are given in Table S1, the results show that they had similar anatase and rutile phases (43 and 57%, respectively) with an average size of 9.7 nm (TNPs—10 nm), which was used for further studies. To make sure that the as-prepared TNP (10 nm) powder has only anatase and rutile crystalline structures, Raman spectroscopy was performed. According to the investigation of Tompsett et al. on the Raman spectrum of TiO_2,[30,31] the Raman spectrum of the as-prepared TNPs in Figure 1b is in good agreement with the XRD result, where only anatase and rutile oscillation modes were recorded. There are four anatase (A) and one rutile (R) peaks in Figure 1b including, a very strong peak of A-E_g at 150 cm^{-1}, an A-B_{1g} peak at 402 cm^{-1}, an A-A_{1g} peak at 516 cm^{-1}, an A-E_g peak at 639 cm^{-1}, and a rutile complex peak (R*) assigned to phonon scattering in the rutile phase at 250 cm^{-1}. All recognized peaks

DOI: 10.1021/acsomega.8b02084
ACS Omega 2019, 4, 146−158

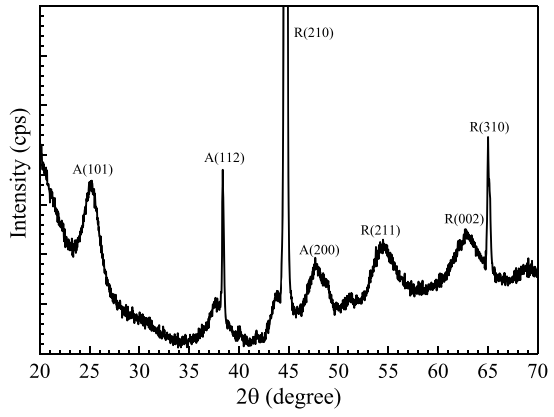

(a)

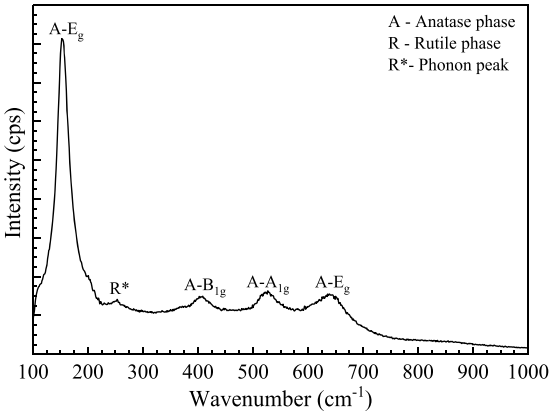

(b)

Figure 1. TNPs' crystalline structure characterized by (a) X-ray diffraction pattern and (b) Raman spectroscopy.

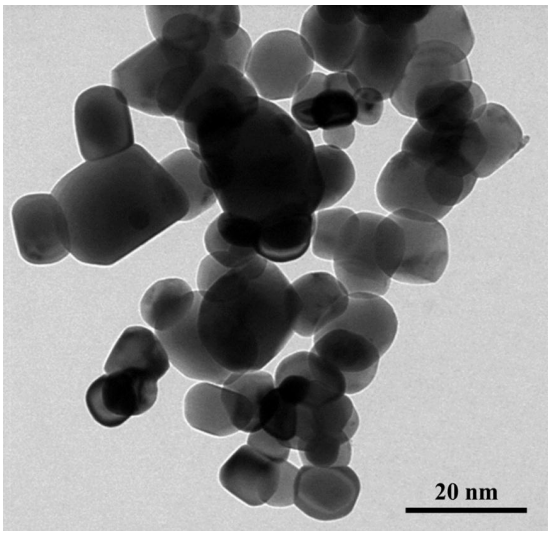

(a)

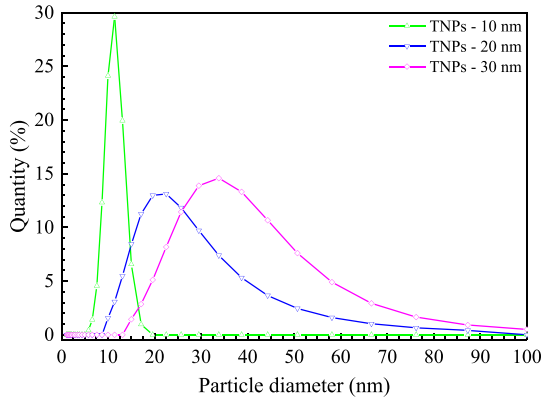

(b)

Figure 2. (a) TEM image of TNPs with 10 nm in diameter and (b) the DLS profile of TNPs dissolved in ethanol.

shifted to higher frequency in comparison to the previous reports, which may be due to structural imperfections present in TNPs.

The diameter of TNPs plays a crucial role in determining their functional ability as effective inhibitors with synergistic effects in the presence of APLE in SEFB medium. To study the particle size of TNPs, scanning electron microscopy (SEM), transmission electron microscopy (TEM), and dynamic light scattering (DLS) measurements were undertaken, as shown in Figures 2 and S1. First, it is observed from SEM images of TNPs (10, 20, and 30 nm) to have corresponding average particle sizes of 11.4, 23.0, and 32.5 nm as shown in Figure S1. Second, the TEM image of TNPs (10 nm) (Figure 2a) shows that the average particle size is about 10.5 nm. Third, DLS profiles in Figure 2b point out the average size of TNPs (10, 20, and 30 nm) as 10.5, 22.5, and 33.8 nm with the highest related proportion of 29.7, 13.2, and 14.5%, respectively. SEM images and DLS result of TNPs are well matched, confirming the sizes of the TNPs as 10, 20, and 30 nm.

To study the inhibitor effects, an immersion test was carried out and studied by SEM measurement for three specimens immersed in different solutions, such as without inhibitor (Figure S2a), with 1000 ppm APLE (Figure S2b), and with 1000 ppm APLE and 30 ppm of TNPs (10 nm) (Figure S2c). The results showcase significant change in samples' surface for the uninhibited and inhibited conditions. Notably, the specimen without protection in Figure S2a shows the discontinuous surface containing many large islands and pinholes that can be attributed to rusting products after the corrosion process. Besides, Figure S2b shows the smoother surface containing some small islands and very few pitting holes, it is obvious to see grinding traces on the surface allowing a thin layer to form above the surface, that can be assigned to APLE. In addition, there is no pitting hole or island on the steel surface as well as there are more organic materials concentrated on the pitting site than the surroundings as observed in Figure S2c, indicating that the APLE and TNP mixture acts synergistically to show better performance as a selective inhibitor. To further understand the composition of this thin barrier layer X-ray photoelectron spectroscopy (XPS) measurements were carried out.

XPS analysis was employed to investigate elemental compositions on the steel surface after 24 h of immersion in SEFB solution without and with APLE and nanoparticle additions as displayed in Figure 3. We investigated surficial films under three immersion conditions including SEFB solution without inhibitor, with 1000 ppm APLE, with 1000 ppm APLE and 30 ppm TNPs, respectively. The wide range of XPS spectra (Figure 3a) exhibits higher Fe peaks, lower C 1s, and O 1s peaks of samples in SEFB without inhibitor

DOI: 10.1021/acsomega.8b02084
ACS Omega 2019, 4, 146−158

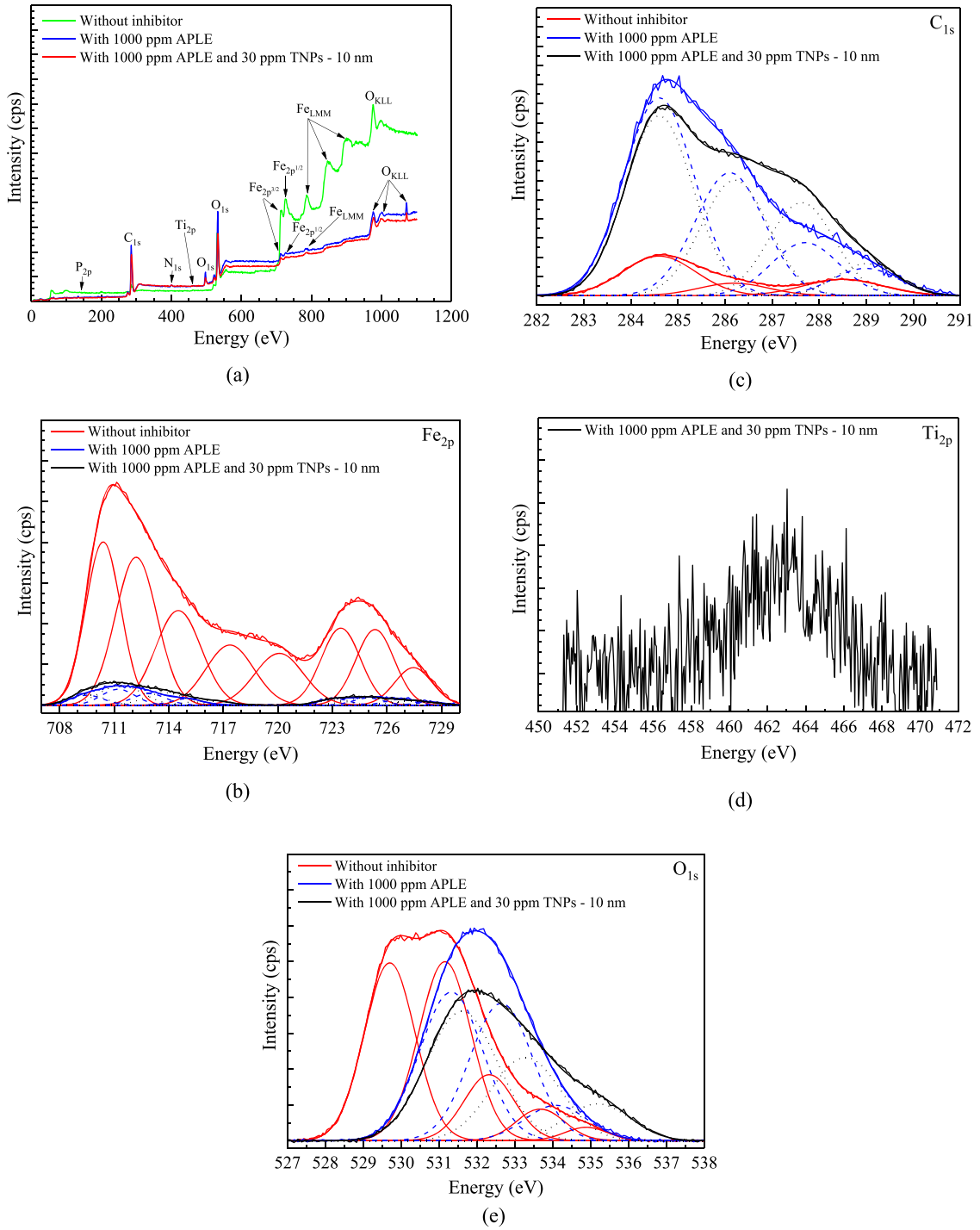

Figure 3. (a) Survey scan spectra and narrow scan spectra of (b) Fe 2p, (c) C 1s, (d) Ti 2p, and (e) O 1s coverage of the steel surface were characterized by XPS measurement.

(uninhibited conditions) compared to those with inhibitor. Besides, the appearance of O 1s (another peak), N 1s, P 2p, and Ti 2p peaks in the inhibited conditions is due to the presence of organic molecules in APLE and TNPs, approving that the inhibitors were covalently linked to the steel surface and mitigated corrosion reactions. The high-resolution spectrum of Fe 2p (Figure 3b) shows strong peaks of rusting products (FeO, Fe_3O_4, Fe_2O_3, and FeOOH) in the uninhibited conditions, whereas they are insignificantly observed in the inhibited conditions. As observed in Figure 3c, the significantly high intensity of the C 1s peak in the inhibited conditions can be contributed to the APLE addition, whereas the lower C 1s peak of uninhibited conditions indicates the presence of organic contamination from the SEFB environment. The high-resolution spectrum of O 1s peaks in Figure 3e indicates that the products on the steel surface included oxide (at 529.7 and 531.1 eV) and hydroxyl (at 532.3 and 533.7 eV) phases in the uninhibited conditions; they were observed around 531.3, 532.6, and 534.2 eV for the specimen immersed in the inhibited systems. The shifts in the peak position suggest the replacement of the chemical bond from iron oxide states in the uninhibited conditions by organic bonding states in the

DOI: 10.1021/acsomega.8b02084
ACS Omega 2019, 4, 146−158

inhibited conditions. Besides, both the Ti 2p peak in Figure 3d and the Ti−O peak at 531.6 eV in Figure 3e confirm the existence of TNPs in the protective layer of APLE and TNP mixture conditions. The XPS data thus showed that the inhibitors formed a film on the samples' surface by creating a chemical bond to the steel substrate, protecting the steel surface from the corrosive environment, thereby significantly reducing the formation of rusting products.

To understand the electrochemical reactions taking place on the steel surface under different conditions, electrochemical impedance spectroscopy (EIS) was performed. It is a modern, highly accurate technique that is used to investigate the existence, character, and formation of protective layers. It is also a useful method to not only study the interface between the coating film and the substrate but also understand the kinetics of the corrosion process. This method is non-destructive towards the sample surface and does not alter the erosion potential. Figure 4a shows Nyquist plots of samples in the blank solution and in the inhibited solutions containing 1000 ppm APLE and 30 ppm TNPs with average size variations. In addition, Nyquist plots of samples in the inhibited solutions containing 1000 ppm APLE without and with various 10 nm-sized TNPs concentrations are presented in Figure 4b. The clear observation of each two-semicircle-shaped loop in Figure 4 indicates the deposition of the protective layer. First semicircles (nature of coatings) show not much distinction, in contrast to the marked distinctions in second semicircles (nature of the double layer formed between the film and the steel substrate). Equivalent circuit in Figure S3 was used to fit the Nyquist plots and respective fitted data are listed in Table S2, where R_s is solution resistance, CPE_{pro} is the constant phase element of the protective film in inhibited conditions, R_{pro} is the resistance of the pores in the film (CPE_{pro} and R_{pro} were replaced by CPE_{rust} and R_{rust} in uninhibited conditions), CPE_{dl} is the constant phase element of the double layer, and R_{ct} is the resistance of the charge transfer between the protective film and the steel substrate, respectively. In electrochemistry, a constant phase element (CPE) represents an imperfect capacitor that has two quantities including Q and α, which represents the capacitive value and mathematical coefficient between 0 and 1. If $\alpha = 0$, the CPE presents pure resistance properties; in the case of $\alpha = 1$, the CPE presents pure capacitor properties; and when $\alpha = 0.5$, the CPE presents half-capacitor and half-resistance properties.

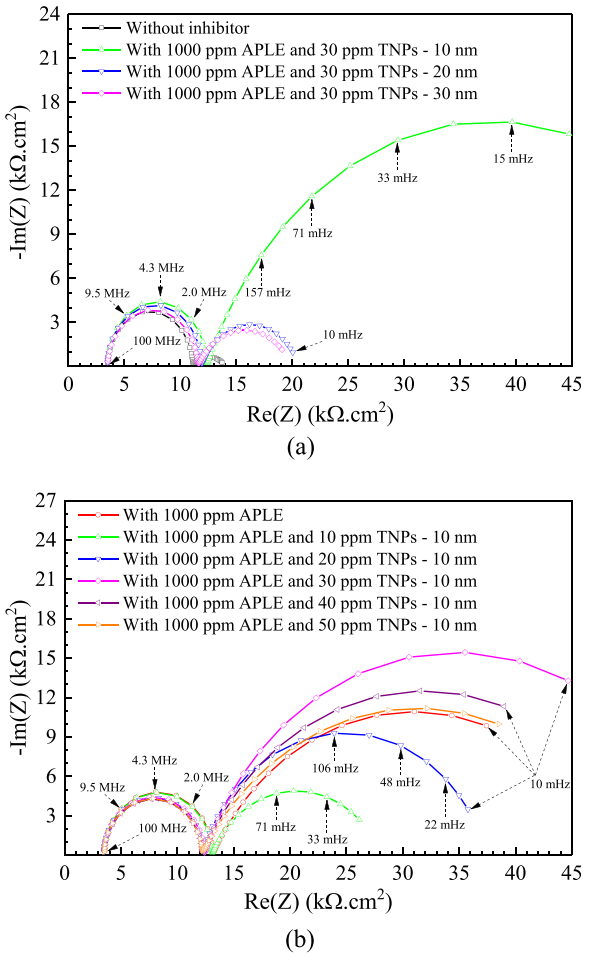

Figure 4. Nyquist plots of steel specimen immersion in solutions (a) without inhibitor and with 1000 ppm APLE in a mixture with different diameters of 30 ppm TNPs and (b) with 1000 ppm APLE in a mixture with different concentrations of 10 nm TNPs.

EIS fitted results in Table S2 show the gradual decrease in the electrical properties of the protective film (represented by R_{pro} and Q_{pro}) and the properties of the interaction between the film and the substrate (represented by R_{ct} and Q_{dl}) with the gradual increase in the TNP size. To be more specific, R_{pro} and R_{ct} decrease whereas Q_{pro} and Q_{dl} increase with the increase in the TNP diameter, besides, the α values as shown in Table S2 decreased showing that their films lose their insulation properties at bigger TNP size. EIS parameters of the TNP (10 nm) sample are the best in the survey, as can be seen, TNPs with 10 nm diameter is the most suitable synergistic conditions in combination with APLE, hence, further studies were carried out with TNPs (10 nm) to examine the influence of TNP concentrations. In addition, for EIS fitting parameters in the case of 0 ppm (without protection of inhibitors), the electrochemical properties of the deposited layer including rusting products are very poor as well as the bonding properties of this coating to the substrate are not good, in comparison with 1000 ppm. As the concentration of TNP (10 nm) inhibitors increases from 10 to 50 ppm, we observe the following, the properties of the coating (characterized by Q_{pro}, α_1, and R_{pro}) and the double layer (characterized by Q_{dl}, α_2, and R_{ct}) increases if TNPs concentration is below 30 ppm, reaches maximum at 30 ppm, and decreases if TNP concentrations are above 30 ppm. All fitting data have low relative error (χ^2 below 0.5), indicating very good fitting quality with the proposed equivalent circuit. Therefore, EIS results elucidated that the TNP's diameter of 10 nm and a concentration of 30 ppm are optimal parameters to act as a synergistic inhibitor in the presence of APLE. The mechanism and characteristic parameters of corrosion and inhibition were further studied through potentiodynamic polarization (PD) measurement.

The potentiodynamic polarization method could provide useful information regarding the mechanism of corrosion as well as corrosion inhibition, which can extrapolate diverse parameters that characterize the corrosion process including corrosion potential, corrosion current density, corrosion rate, inhibition efficiency, and polarization resistance. We studied potentiodynamic polarization curves of carbon steel immersed in SEFB composed of 1000 ppm APLE combined with 30 ppm TNPs with varied particle diameter as shown in Figure 5a,

DOI: 10.1021/acsomega.8b02084
ACS Omega 2019, 4, 146−158

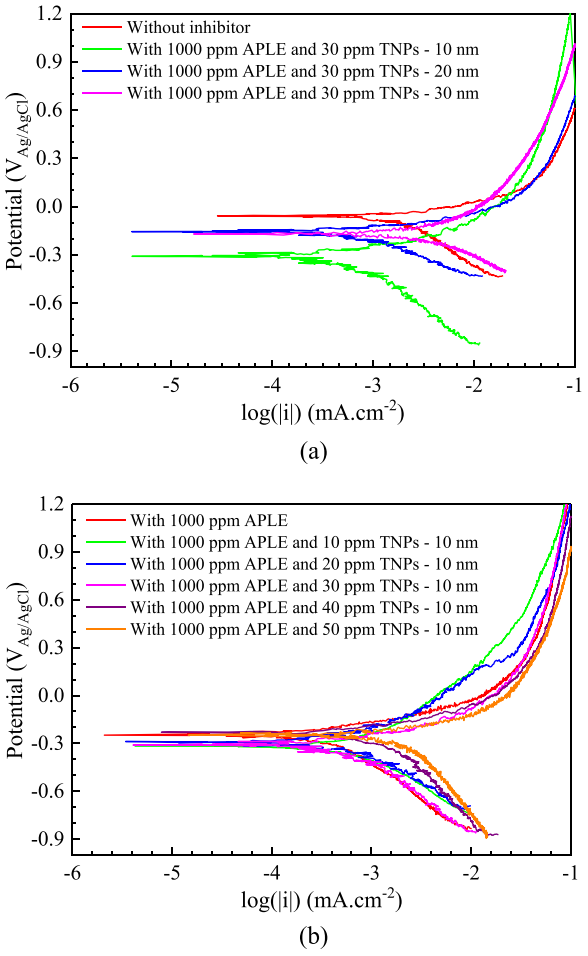

Figure 5. Potentiodynamic polarizations of steel in solution (a) without inhibitor and with 1000 ppm APLE in a mixture with different diameters of 30 ppm TNPs and (b) with 1000 ppm APLE in a mixture with different concentrations of 10 nm TNPs.

whereas the Tafel plot of inhibited solutions containing 1000 ppm APLE without and with different concentrations of 10 nm TNPs are displayed in Figure 5b. Table 1 lists Tafel fitted parameters of samples in Figure 5, herein the polarization resistance, corrosion rate, and inhibition efficiency were calculated using the formulas 1−3, respectively.[32] The results for the corrosion rate and inhibition efficiency as a function of TNP diameter and concentration are shown in Figure S4.

$$R_p = \frac{1}{i_{corr}} \times \frac{\beta_a \beta_c}{2.303(\beta_a + \beta_c)} \quad (1)$$

$$CR = \frac{i_{corr} \cdot k \cdot EW}{d \cdot A} \quad (2)$$

$$IE\ (\%) = \frac{i^0_{corr} - i_{corr}}{i^0_{corr}} \times 100\% \quad (3)$$

To be more specific, in eq 1, R_p is the polarization resistance in kΩ, i_{corr} is the corrosion current density in μA/cm^2, β_a and β_c are the anodic and cathodic Tafel constant in mV; in eq 2, CR is the corrosion rate in mm/y, $k = 3.27 \times 10^{-3}$ is a constant that specifies the units for the corrosion rate in mm, $d = 7.85$ g/cm^3 is the density of steel, EW = 28.25 g/mol is the equivalent weight of steel, and A is the exposed area in cm^2; in eq 3, IE (%) is inhibition efficiency, i^0_{corr} and i_{corr} are the corrosion current density of the uninhibited system and inhibited systems in μA/cm^2, respectively. The PD results displayed in Table 1 have good consistency with EIS results in Table S2 with respect to corrosion protective capability of APLE and TNPs. The mixture of APLE and TNPs exhibits mixed inhibition characteristics as observed from the change of both the slope of anodic and cathodic branches. The slopes of both branches reach their lowest values for TNPs with 10 nm diameter and 30 ppm concentration. Besides, corrosion potentials and corrosion current densities (E_{corr} and i_{corr}) of specimens increase with increasing TNP size or concentration beyond 30 ppm. They also show the decline when increasing TNP (10 nm) concentration from 0 to 30 ppm. It might be due to the considerable effect of the inhibitor layers on the current flows. This showcases that the smaller the value of E_{corr} and i_{corr} are, the greater the polarization resistance (R_p) of the layer is. Extrapolating results of R_p, IE, and CR in Table 1 and Figure S4 show that the maximum R_p value (64 kΩ), highest IE value (97%), and minimum CR value (0.008 mmpy) are observed by using 10 nm sized TNPs at 30 ppm concentration. Next, to explain APLE's protective mechanism in synergy with TNPs, few characterization methods were carried out as explained in the below section.

Gas chromatography−mass spectrometry (GC−MS) is a widely applied method to probe the organic constituents derived from plant extracts. The result of GC−MS of the as-prepared *A. polymorphum* leaf−ethyl acetate extract against retention time is exhibited in Figure 6. Apparently, despite being tracked within 55 min, APLE can only be recorded at the final stages of the isolation process from 32nd to 42nd min,

Table 1. Corrosion Properties from the Potentiodynamic Polarization Curves of Carbon Steel Immersed in the Investigated Solution Containing 0 and 1000 ppm APLE with Different Concentrations of 10 nm TNPs, and 1000 ppm APLE with 30 ppm TNPs of 10, 20, and 30 nm in Diameter

	E_{corr} ($mV_{Ag/AgCl}$)	i_{corr} (μA cm^2)	β_a (mV/decade)	$-\beta_c$ (mV/decade)	χ^2	R_p (kΩ)
0 ppm	−64	5.3	464	386	74	13
1000 ppm	−264	0.4	145	93	100	58
1010 ppm-10 nm	−245	0.7	190	129	439	51
1020 ppm-10 nm	−241	0.5	166	87	92	56
1030 ppm-10 nm	−299	0.3	106	84	87	64
1030 ppm-20 nm	−136	2.2	128	401	132	21
1030 ppm-30 nm	−125	3.3	132	437	120	17
1040 ppm-10 nm	−245	0.5	112	100	382	46
1050 ppm-10 nm	−260	0.7	233	133	60	56

DOI: 10.1021/acsomega.8b02084
ACS Omega 2019, 4, 146−158

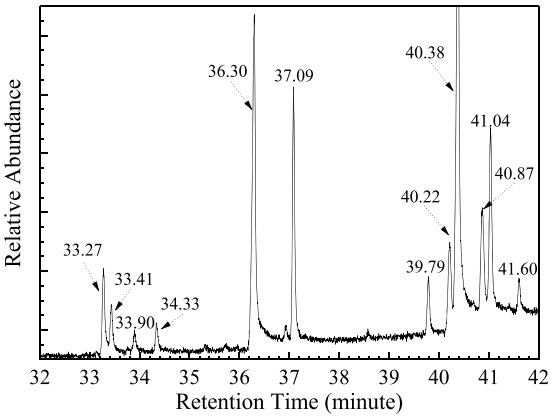

Figure 6. Gas chromatography spectrum of the as-prepared APLE.

whereas the equipped silica column can more easily adapt low polarized compounds rather than high ones. It means this green extract is of excellent compatibility with ethanol blended gasoline. The peaks included eight primary signals and some negligible signals. When compared with commercial spectroscopy library NIST 2.0, the phytochemical structures were found to be consisting of (1*R*)-1-cyclohexylethanamine, hexadecanoic acid (HA), ethyl hexadecanoate (EH), (1*S*)-1-cyclohexylethanamine, ethyl (9*Z*,12*Z*)-hexadeca-9,12-dienoate, octadeca-9,12,15-trienoic acid, propan-2-yl 16-methylheptadecanoate, and ethyl (9*E*,12*E*,15*E*)-octadeca-9,12,15-trienoate. The correlation between the GC−MS data with Fourier transform infrared (FT-IR) data of both the as-prepared glue and steel surface after immersion, demonstrates the effective participation of organic functional groups in inhibiting action. The selected compounds, hexadecanoic acid and ethyl hexadecanoate, were used to carry out simulation studies as they were recognized by the NIST GC−MS Search 2.0 software with very high probability (approximately 70%), whereas the others had lower probability (below 30%). The obtained results could help in understanding the electronic and adsorptive characterization of the APLE inhibitor upon interaction with the steel substrate. In addition, our previous research[11] on the FT-IR spectrum of the as-prepared APLE revealed the existence of the O−C═O groups, the C═O bond, the C−H bending mode in the methyl group, and the aliphatic C−H group that are very consistent with the GC−MS result. Therefore, FT-IR results further confirmed two selected substances (hexadecanoic acid and ethyl hexadecanoate) of APLE.

Ab initio simulation is a state-of-the-art approach to study the detailed molecular structures, their physical−chemical properties, and the microscopic interactions between them at a microscale or nanoscale. Correlating this with the experimental results can help us to understand the nature of many processes that may not be possible otherwise. To mimic the real environment of corrosion, previous reports[33−39] suggested that MD simulation should be carried out in the presence of all concerned species which will actually take part in corrosion inhibition processes such as H_2O, H_3O^+, inhibitor molecules, and the Fe surface. However, this study involves a more complicated corrosion system that cannot be simulated. Therefore, MD simulation was performed to understand the adsorption behavior as well as the interaction between the two inhibitor molecules (hexadecanoic acid and ethyl hexadecanoate) and the Fe(110) surface under the influence of temperature (at 25 and 60 °C, equal to 298 and 333 K). These molecules were analyzed by density functional theory (DFT) to evaluate their quantum chemical properties. In the DFT study of inhibitor molecules,[40] E_{HOMO} and E_{LUMO} are very important quantum chemical parameters. According to the frontier molecular orbital theory, the highest occupied molecular orbital (HOMO) is filled orbitals that have the ability to give electrons to the metal (iron) surface and the lowest unoccupied molecular orbital (LUMO) is empty orbitals of the inhibitor molecules that have the ability to accept electrons from iron atoms. From Koopman's theorem, E_{HOMO} and E_{LUMO} are closely related to the ionization potential (I) and electron affinity (A), namely

$$I = -E_{HOMO} \tag{4}$$

$$A = -E_{LUMO} \tag{5}$$

Therefore, a gap between E_{LUMO} and E_{HOMO} is defined as the energy gap (ΔE), its physical meaning is the stability index of a molecule, which means the smaller the ΔE value, the higher the reactivity of the molecule to absorb on iron surface is. ΔE is calculated by

$$\Delta E = E_{LUMO} - E_{HOMO} \tag{6}$$

On the basis of the hard and soft acid and base theory (HSAB), inhibitor molecules and iron atoms can be considered as Lewis base and Lewis acid, relatively. Pearson extended HSAB theory by giving global hardness quantity, herein, the global hardness (η) represents the ability of an atom to resist charge transfer. Besides, electronegativity (χ) is the inferred parameter to characterize the ability of attracting electrons of an atom in a chemical bond with another atom. η and χ are obtained by formulas 7 and 8. Using η and χ, the fraction of electron transfer from inhibitor molecules to the iron surface (ΔN) is given by eq 9.

$$\eta = \frac{I - A}{2} \tag{7}$$

$$\chi = \frac{I + A}{2} \tag{8}$$

$$\Delta N = \frac{\chi_{Fe} - \chi_{inh}}{2(\eta_{Fe} + \eta_{inh})} \tag{9}$$

In recent years, the value of χ_{Fe} in eq 9 has been suggested to be replaced by work function (Φ) values[41] but this has not been widely accepted as well as there are many issues needing further discussion with this replacement. Therefore, χ_{Fe} = 7 eV and η_{Fe} = 0 eV were chosen for eq 9 as suggested by various reports.[42−44] Ju et al.[45] showed that any positive value of ΔN below 3.6 indicated electron transfer from the inhibitor molecule to the metal surface, on the other hand, negative values of ΔN indicated electrons transfer from the metal surface to the inhibitor molecule. The Fukui function is an important parameter to the determined local selectivity of an inhibitor, showing which part of the molecule tends to be more attractive to electrons or ions. The electrophilic $f(-)$ or nucleophilic $f(+)$ Fukui function represents the changes in electron density of the molecules when they lose or gain electrons, the higher values of $f(-)$ or $f(+)$ could reflect the higher ability to donate or accept electrons.

Hexadecanoic acid (HA) and ethyl hexadecanoate (EH) were considered as the main component of APLE, they were

DOI: 10.1021/acsomega.8b02084
ACS Omega 2019, 4, 146−158

Table 2. Simulation Data Calculation[a]

(a)

	E_{HOMO} (eV)	E_{LUMO} (eV)	ΔE (eV)	I (eV)	A (eV)	χ (eV)	η (eV)	ΔN
HA	−6.845	0.768	7.613	6.845	−0.768	3.807	3.039	0.520
EH	−6.603	0.973	7.576	6.603	−0.973	3.788	2.815	0.552

(b)

temperature (°C)	E_b of HA/Fe(110) (kcal/mol)	E_b of EH/Fe(110) (kcal/mol)	E_{tot} of HA/Fe(110) (kcal/mol)	E_{tot} of EH/Fe(110) (kcal/mol)
25	−18 573	−22 369	−98 319	−118 282
60	−18 574	−22 371	−98 318	−118 280

[a](a) DFT calculation of optimized HA and EH molecules. (b) Binding energy (E_b) of HA and EH on Fe(110) at 25 and 60 °C.

first deposited onto the steel substrate due to their inhibiting properties. When the porous organic layer formation reached enough thickness, TNPs could be attracted and entangled to the pores inside that layer, thereby filling the pores and preventing aggressive materials to pass through the organic layer. There are two separated interactions in the model which are, first, the interaction between the organic layer and the iron surface that directly effects the experimental results, and finally, the interaction between HA and EH with TNPs, which is complicated and has an indirect effect on the experimental results, consequently this type of interaction can be ignored. DFT calculation was applied for hexadecanoic acid (HA) and ethyl hexadecanoate (EH) molecules using the DMol3 module. Figure S5 shows the HOMO (a), LUMO (b), nucleophilic (c), and electrophilic (d) distribution of geometry optimization of HA and EH molecules. As can be observed, the molecules of both the HOMO and LUMO as well as $f(+)$ and $f(-)$ are allocated around the carbonyl functional group. From Figure S5a,b, both the HOMO regions spread on the xOy plane, whereas the LUMO regions are both oriented to the Oz direction. In contrast, Figure S5c,d revealed that both nucleophilic sites oriented to the Oz direction, whereas electrophilic sites are expanded to a direction on the xOy plane but only positioned at around the oxygen atom in the C═O bond. As a result, it is expected that HA and EH molecules prefer adsorbing on the Fe(110) surface by the xOy plane; hence, the adsorption configuration of inhibitors on the Fe(110) surface are set horizontally. Other simulation parameters are presented in Table 2a. Both HA and EH having positive ΔN values indicate that electrons have transferred from inhibitor molecules to the Fe(110) surface and reduced the formation of iron ions. In comparison with HA, EH has higher E_{HOMO}, lower E_{LUMO} and η, whereas other parameters are almost the same, suggesting EH to donate electrons to the Fe(110) surface. Additionally, EH has a ΔN value (0.552) higher than HA's (0.520). From the above, it can be interpreted that EH could be a better inhibitor than HA.

To determine the absorption configuration in MD simulation, two simulation boxes were created, one contained a 12 × 9 supercell of Fe(110) and a hexadecanoic acid molecule with a size of 34.40 × 36.48 × 41.44 Å^3, the other contained a 13 × 10 supercell of Fe(110) and an ethyl hexadecanoate molecule with a size of 37.26 × 40.54 × 44.77 Å^3. Before thermodynamics calculation, each structure in the simulation boxes performed geometry optimization to find appropriate sites as well as spatial orientations of the molecules above the steel surface. The optimization process eliminated unreasonable configurations, resulting in more reliable subsequent calculations. After thermodynamics calculation, the total energy of configurations was obtained, whereas binding energy between the inhibitor molecules and the Fe(110) surface were calculated by

$$E_{int} = E_{tot}^{(surface+inhibitor)} - (E_{tot}^{surface} + E_{tot}^{inhibitor}) \quad (10)$$

$$E_{bind} = -E_{int} \quad (11)$$

In eq 10, $E^{surface}$, $E^{inhibitor}$, and $E^{(surface+inhibitor)}$ are the total energy of, Fe(110) supercell, HA and EH molecules, and simulation boxes that contain Fe(110) supercell plus inhibitor molecules, respectively. In eq 11, E_{int} is the interaction energy, E_{bind} is the binding energy between the inhibitor molecules and the Fe(110) surface. Adsorption equilibrium configuration of HA and EH on the Fe(110) surface at 25 and 60 °C are presented in Figure 7, whereas calculated binding energies are listed in Table 2b. Figure 7 shows both HA and EH at their most stable (lowest energy) configuration as well as at the Fe(110) surface after the simulation process, which indicates that they have good adhesion to the steel substrate. In combination with the binding energy of HA and EH from Table 2b, we can observe that both HA and EH have high binding energy to the Fe(110) surface, and the binding energy of EH is higher than HA, resulting in better adhesion to the steel substrate, that are consistent with the previous prediction. In addition, the increases in total energies of both HA and EH from Table 2b with increasing temperature show that the adsorption of these inhibitors to the steel substrate is an endothermic process, indicating that the adsorption of HA and EH on steel substrates could be attributed to chemisorption. Because of the changes of total energies with temperature (1 kcal/mol of HA and 2 kcal/mol of EH per 35 °C), it can be concluded that HA and EH are very stable inhibitors for the steel substrate, indeed, by using energy to heat conversion (the change of 1 kcal/mol is equivalent to the change of 503 K), from the change of total energy by temperature as above, we can estimate that the adsorbent films are stable up to 563 °C for HA and 1063 °C for EH.

Two organic compounds present in APLE are hexadecanoic acid (HA) and ethyl hexadecanoate (EH), they are considered to be the main component in APLE. They adsorb onto the steel surface and form a protective layer having a complex structure (long and hydrophobic hydrocarbon chains) with a mesoporous network (porous structures with pore sizes of about tens of nanometer). These pores allow passage of corrosive agents from SEFB to penetrate through the film via the grain boundary (channel) formed by imperfections in the steel structure. These corrosive agents can easily access and attack the steel surface, resulting in the reduction of protection effectiveness. With the low APLE concentration (100 ppm), inhibitors bind to the steel surface in the form of discrete distribution clusters with rusting products and cannot fully

DOI: 10.1021/acsomega.8b02084
ACS Omega 2019, 4, 146−158

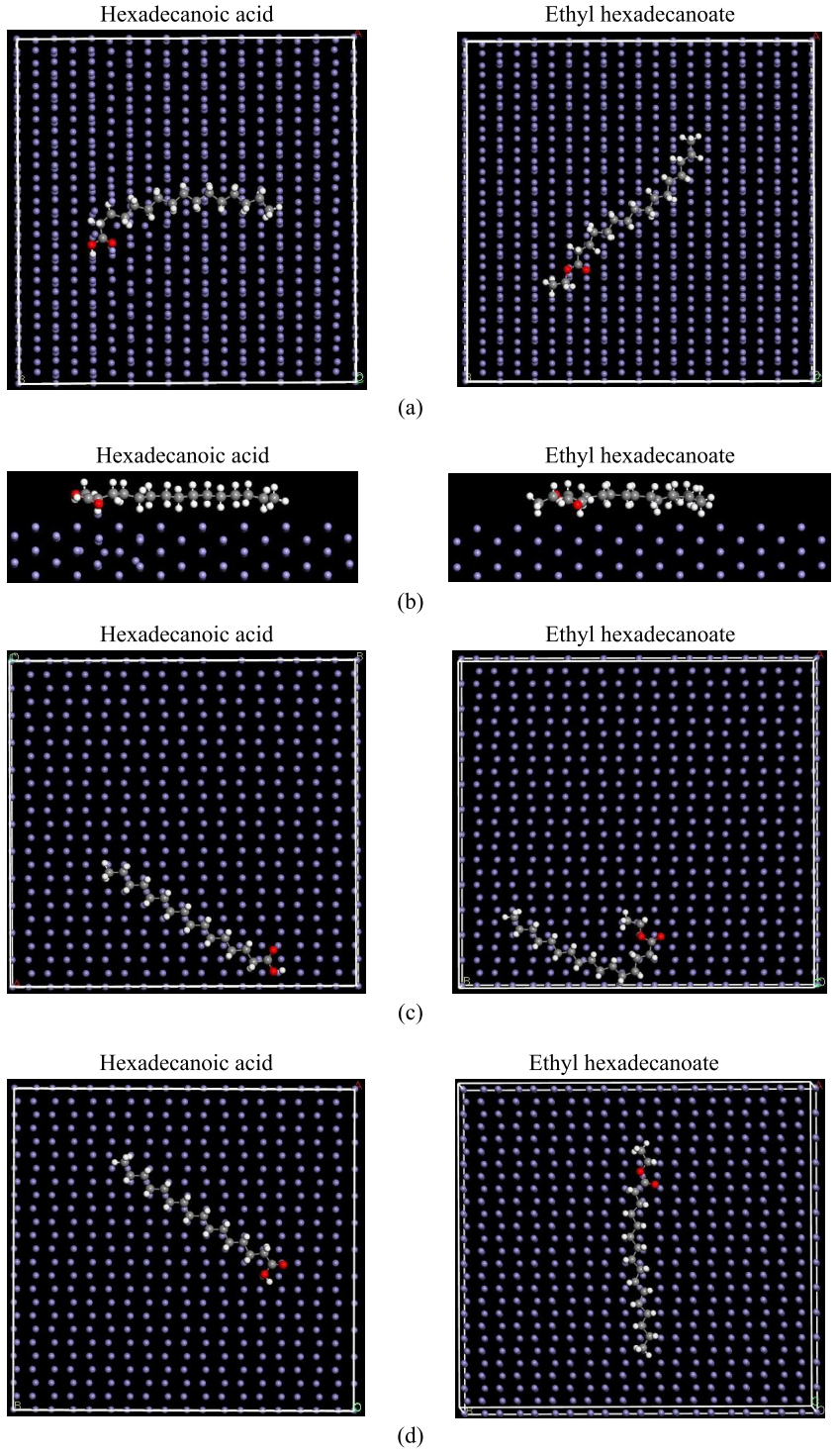

Figure 7. Equilibrium adsorption configurations of HA and EH on the Fe(110) surface from MD simulations. (a) Top view, (b) side view, (c) top view at 25 °C and (d) at 60 °C.

cover the surface. With the higher APLE concentration (500 ppm), the coating can cover the steel substrate surface completely, but the material density was still low with the large size of channels and pores. When the APLE concentration reached 1000 ppm, the material density in the film became sufficient to minimize the number as well as the size of channels and pores, leading to a maximum protective effect.[11] However, the coating was thicker and the disorder in the structure increased when adding inhibitor concentrations beyond 1000 ppm, resulting in a sharp increase in the number of small size channels and pores that reduce protection. The protective mechanism of TNPs in a mixture with APLE indicated that the optimized size (10 nm) and concentration (30 ppm) of TNPs with the appropriate size (10 nm of diameter) and concentration (30 ppm) effectively filled the pores and channels in the APLE's network to curb the penetration of corrosive agents from SEFB into the coating structure, thereby increasing the protective effect. In the case of

DOI: 10.1021/acsomega.8b02084
ACS Omega 2019, 4, 146−158

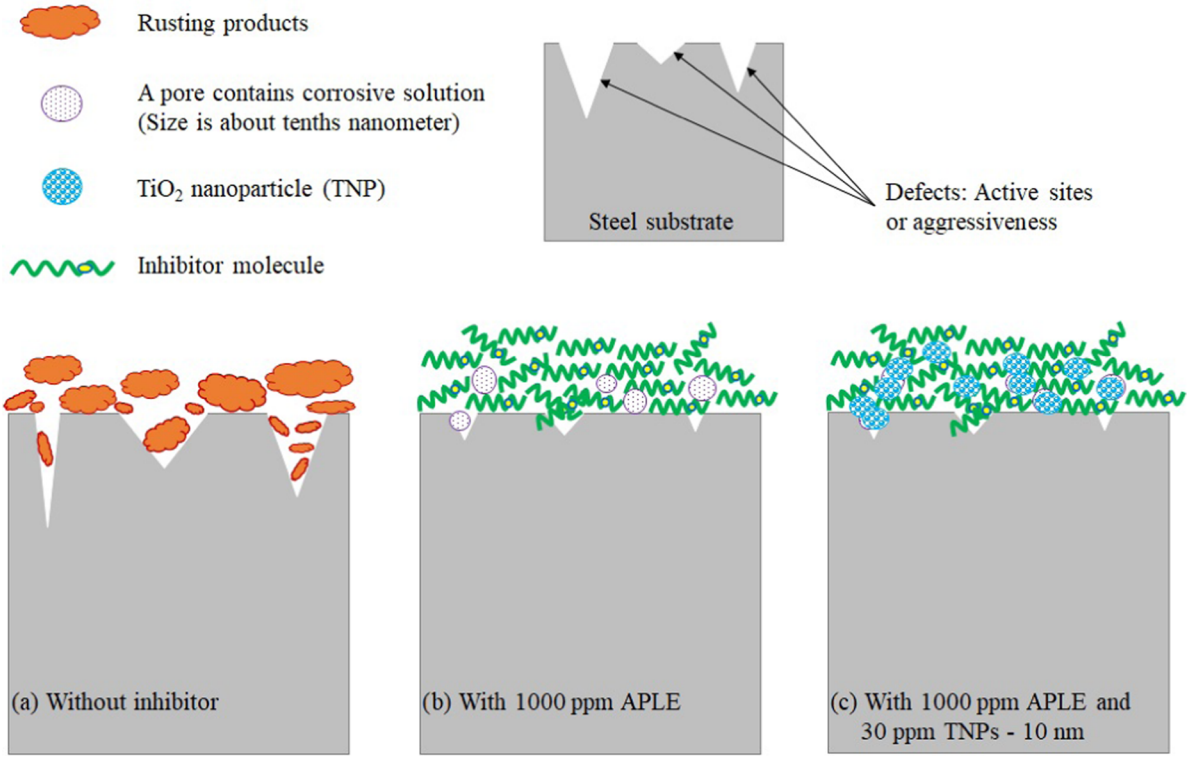

Figure 8. Proposed schemata of (a) corrosion process and inhibition mechanism of (b) APLE and (c) APLE in the mixture with TNPs.

larger TNP size (20 and 30 nm), the incompatibility of the TNP size with the pores and channels in the film structure, unfortunately, led to the breakdown in continuity of the coating, creating many secondary channels and pores of large sizes, resulting in the decrease in the protective effect. In the case of low concentrations of TNPs (10 and 20 ppm), the amount of TNPs was not sufficient to fill the pores. At small sizes, they can easily diffuse from the interior pores to surface coating due to concentration difference. In addition, the corrosive agents from SEFB migrated from the surface to interior pores following TNPs' pathways. With high concentrations of TNPs (40 and 50 ppm), high density of TNPs reduced the density of APLE in the film; as a result, the coating became more porous with the expanded pores and channels, allowing corrosive agents from SEFB to penetrate more easily to the coating. All of the above-mentioned protection mechanisms of APLE and APLE−TNPs mixture is summarized and illustrated in Figure 8. Finally, this work has shown that TNPs with 10 nm of diameter and 30 ppm of concentration mixed with 1000 ppm APLE inhibitor have improved properties to form a protective layer, which greatly enhanced the protective effect of the composite film in the SEFB environment, thereby showcasing the characteristics of a synergistic inhibitor for improving the steel corrosion resistance.

3. CONCLUSIONS

A new approach for corrosion protection suggested in the present work proposes the self-healing ability of TNPs for blocking the defects in an organic protective film formed on the metal surface along with the use of organic corrosion inhibitors. Controllable inhibition efficiency of steel was successfully gained via incorporation of TNPs and APLE as synergistic inhibitors in the SEFB medium. The TNPs were incorporated with APLE molecules to form the protective film that acted as a heat stable barrier layer on the steel surface, resulting in improved corrosion resistance as confirmed by DFT and MD simulation. Smaller nanosized titania with an optimal concentration served as the better corrosion inhibitor for steel in the investigated solution due to its ease of passing through the defects on the protective film. These phenomena resulted in significant reduction of corrosion current densities and enhanced surface resistances of steel after immersion in investigated solution. In addition, the study also indicated that the nanoparticles with the synergistic inhibition properties are very important in defect filling ability for corrosion protection of metals. It could create a new approach to fight the drawback of organic corrosion inhibitors, suggesting an expansion of the next generation of corrosion protection systems.

4. MATERIALS AND METHODS

APLE was produced by the Soxhlet extraction process, the detailed process was presented in the previous report.[11] In short, fresh *A. polymorphum* leaves were dried at 60 °C, triturated to powder, and was added to a Soxhlet extractor containing ethyl acetate, and then extracted at 75 °C for 24 h. In the following step, the extract (APLE) was filtered, concentrated, and stored in a dry cabinet at room temperature. The extracted product was analyzed by an attenuated total reflectance Fourier transform infrared spectroscopy apparatus (α-FT-IR spectrometer), coupled with gas chromatography−mass spectroscopy (GC−MS) (Agilent 7890B for GC and Agilent 5977A for MS). The GC−MS probe was equipped with a silica column (30 m of length, 0.25 mm of diameter) with the mobile phase flow rate of 1 mL/min, under helium as the carrier gas and split ratio of 10:1. The injector temperature and detector temperature were 250 and 280 °C, respectively. The oven temperature settings were conducted at 60 °C,

DOI: 10.1021/acsomega.8b02084
ACS Omega 2019, 4, 146−158

Table 3. Steel Components Determined by Optical Emission Spectroscopy

chemical elements (wt %)														
C	Mn	Si	S	P	Ni	Cr	Mo	Cu	V	Nb	Ti	Al	B	Fe
0.16	0.73	0.21	0.01	0.02	<0.01	0.03	<0.01	<0.01	0.01	<0.01	<0.01	<0.005	<0.005	bal.

elevated to 220 °C with a step of 4 °C/min. The results of MS spectra were compared with NIST 2.0 Library to identify the chemical structures of the detected compounds of APLE.

TNPs were synthesized by a sol−gel process using tetraisopropyl orthotitanate (TTIP), the entire process was conducted in a glove box containing dry nitrogen at ambient room temperature. All chemicals used in the experiment were of reagent grade, purchased from MERCK Singapore and used directly without further purification. First, 15.00 mL of TTIP (minimum purity 98%) was mixed with 34.15 mL of isopropyl alcohol (IPA, minimum purity 99.8%) and 0.19 mL of diethanolamine (DEA, minimum purity 99.5%) by magnetic stirring at 500 rpm for 4 h, to form 1.0 M precursor solution with a molar ratio of TTIP/DEA being 1:1. Second, 0.07 mL of deionized water (passed ASTM D1193[46]) and 14.01 mL of IPA was stirred at 500 rpm for 4 h for hydrolysis. Third, the first solution was added dropwise to the second solution and simultaneously stirred at 1200 rpm using a magnetic stirrer until the molar ratio of the reactant TTIP/DEA/H_2O/IPA (1:1:4:100) was attained. Finally, TNPs in powder form was washed several times with deionized water to remove any residuals after the synthesis, then dried in a vacuum cabinet, and carefully mashed before using for further characterization. Steel was fabricated, wired and molded by epoxy resin, and finally ground by 2000 grit silicon carbide paper before measuring.

The corrosive medium, simulated ethanol fuel blend (SEFB), was prepared in accordance with ASTM D7577 rating no. 5,[47] containing chemical contents as given in Table S3. In this research, the commercial unleaded gasoline RON92 was used instead of Fuel C. The environments used for this study were SEFB without inhibitor, with 1000 ppm APLE, with 1000 ppm APLE in a mixture with 30 ppm TNPs of different diameters, and with 1000 ppm APLE in a mixture with different concentrations of TNPs of 10 nm in diameter. To prepare the APLE−TNP mixtures, 100 mL SEFB and an appropriate amount of APLE and TNPs were added into closed beakers and magnetically stirred at 900 rpm at 38 °C for 1 h, and then stabilized for 15 min before employing the immersion process in which the steel samples were introduced into the prepared beakers with their metal faces (10 × 10 mm^2 of exposed area) downward. The immersion test lasted 24 h in a closed cabinet. The electrochemical measurements were followed right after the immersion test without any interference in testing solutions.

Electrochemical impedance spectroscopy (EIS) and potentiodynamic polarization (PD) measurements were performed by the VSP Potentiostat instruments. The measurements were taken in the three-electrode electrochemical cell that contains two platinum meshes as the counter electrode, the silver/silver chloride as the reference electrode, and steel samples as the working electrode. In EIS measurement, the peak-to-peak amplitude of the sinusoidal perturbation was 10 mV and the frequency varied from 100 kHz to 10 mHz. The PD measurement was undertaken immediately after finishing EIS, with a scan range from −0.250 V vs an open circuit voltage (E_{OCP}) to +0.800 V vs $V_{Ag/AgCl}$ and a scan rate of 0.166 mV/s. The EIS, PD data and related fitting parameters were processed by integrated EC-Lab software version 10.36.

The steel components were determined by optical emission spectroscopy as given in Table 3. X-ray diffraction (XRD) pattern of TNP powder was examined by Panalytical X'Pert Pro materials research diffractometers. The Raman spectra of TNP powder was recorded in a Horiba Jobin Yvon−Raman Spectrometer. Scanning electron microscopy (SEM) images of TNPs and steel sample surface after 24 h of immersion test were studied by a Hitachi S-4800 field emission scanning electron microscope. The transmission electron microscopy (TEM) image of TNPs powder was inspected by a JEOL JEM-1400 flash transmission electron microscope. Dynamic light scattering (DLS) profile was analyzed by a dynamic light scattering particle size analyzer LB-550-Horiba system. The XPS data of the immersion samples in SEFB without and with inhibitor were dissected by the AES-XPS ESCA-2000 system.

In this research, an ab initio approach was applied to study the interaction between inhibitor molecules and steel substrates. Inhibitor molecules were geometrically optimized in the DMol3 module with the following settings: Becke's 3 parameter exchange Lee Yang and Parr correlation functional (B3LYP), DFT semi-core pseudopotentials core treatment, DNP basis set with basis file 3.5 for an electronic structure, population analysis containing Mulliken orbitals and charge analysis along with Hirshfeld quadrupole analysis, energy and force convergence tolerance were set as 1.0×10^{-5} Ha and 0.002 Ha/Å. Energy calculations were based on optimized structures and respective electronic parameters consisting of the highest occupied molecular orbital energy (E_{HOMO}), the lowest unoccupied molecular orbital energy (E_{LUMO}), energy gap (ΔE), global hardness (η), electronegativity (χ), the fraction of transferred electron (ΔN), and Fukui functions. Besides, the Fe crystal was geometrically optimized in a CASTEP module with generalized gradient approximation, Perdew−Wang 1991 (PW91) exchange−correlation, OTFG ultrasoft pseudopotentials, Koelling−Harmon relativistic treatment, and energy and force convergence tolerance were set as 5.0×10^{-6} eV/atom and 0.01 eV/Å. After optimizing the Fe structure, the Fe(110) surface containing five atom layers was built for the adsorption simulation process, The Fe(110) lattice was chosen because of its popularity in nature, whereas five iron atom layers was chosen to avoid the influence of periodic lattice image on inhibitor molecules. The Fe(110) and inhibitor molecules interaction were carried out by molecular dynamics (MD) simulation in the Forcite module with ultra-fine quality, appropriate boxes with periodic boundary conditions were applied for each inhibitor molecule. During the optimization process, the first and last layer in the Fe(110) surface are constrained and the condensed phase optimized molecular potentials for atomistic simulation studies forcefield were taken into calculation. The MD simulation was performed at 25 °C (298 K) and 60 °C (333 K) under canonical ensemble (NVT) using a time step of 1.0 fs within the total simulation time of 2000 ps. All simulation processes were performed using the BIOVIA Materials Studio package.

DOI: 10.1021/acsomega.8b02084
ACS Omega 2019, 4, 146−158

■ ASSOCIATED CONTENT

Supporting Information

The Supporting Information is available free of charge on the ACS Publications website at DOI: 10.1021/acsomega.8b02084.

TNPs (10 nm) average size and weight fraction calculated from the XRD pattern (Table S1); parameters of electrochemical impedance spectroscopy measurements (Table S2); simulated ethanol fuel blend contents (Table S3); SEM images of TNPs (Figure S1); SEM images of exposed specimens in investigated solutions with different concentration additions (Figure S2); proposed equivalent circuit for fitting the impedance data (Figure S3); effect of (a) TNPs' sizes and (b) TNPs' concentrations on corrosion rate of steel in investigated solution (Figure S4); DFT study of HA and EH isolated optimized molecules (Figure S5) (PDF)

■ AUTHOR INFORMATION

Corresponding Authors

*E-mail: (N.D.M.) nguyendangnam@dtu.edu.vn.
*E-mail: (V.T.H.T.) vththu@hcmus.edu.vn.

ORCID

Nguyen Dang Nam: 0000-0003-4434-0763

Author Contributions

‖N.S.H.V. and P.V.H. contributed equally to this work.

Notes

The authors declare no competing financial interest.

■ ACKNOWLEDGMENTS

This research is funded by the Ho Chi Minh City Department of Science and Technology under grant number 136/2017/HĐ-SKHCN (780/QĐ-SKHCN).

■ REFERENCES

(1) Barbir, F.; Veziroglu, T. N.; Plass, H. J., Jr. Environmental damage due to fossil fuels use. *Int. J. Hydrogen Energy* **1990**, *15*, 739−749.
(2) Shaffer, G.; Steffen, M. O.; Jens, O. P. P. Long-term ocean oxygen depletion in response to carbon dioxide emissions from fossil fuels. *Nat. Geosci.* **2009**, *2*, 105−109.
(3) Nicolotti, G.; Simon, E. Soil contamination by crude oil: Impact on the mycorrhizosphere and on the revegetation potential of forest trees. *Environ. Pollut.* **1998**, *99*, 37−43.
(4) Dincer, I. Renewable energy and sustainable development: A crucial review. *Renewable Sustainable Energy Rev.* **2000**, *4*, 157−175.
(5) Panwar, N. L.; Kaushik, S. C.; Kothari, S. Role of renewable energy sources in environmental protection: A review. *Renewable Sustainable Energy Rev.* **2011**, *15*, 1513−1524.
(6) Nigam, P. S.; Singh, A. Production of liquid biofuels from renewable resources. *Prog. Energy Combust. Sci.* **2011**, *37*, 52−68.
(7) Hsieh, W. D.; Chen, R. H.; Wu, T. L.; Lin, T. H. Engine performance and pollutant emission of an SI engine using ethanol−gasoline blended fuels. *Atmos. Environ.* **2002**, *36*, 403−410.
(8) Pouliot, S.; Babcock, B. A. Feasibility of meeting increased biofuel mandates with E85. *Energy Policy* **2017**, *101*, 194−200.
(9) Hassan, S. N.; Sani, Y. M.; Aziz, A. R. A.; Sulaiman, N. M. N.; Daud, W. M. A. W. Biogasoline: An out-of-the-box solution to the food-for-fuel and land-use competitions. *Energy Convers. Manage.* **2015**, *89*, 349−367.
(10) Jia, L. W.; Shen, M. Q.; Wang, J.; Lin, M. Q. Influence of ethanol−gasoline blended fuel on emission characteristics from a four-stroke motorcycle engine. *J. Hazard. Mater.* **2005**, *123*, 29−34.
(11) Vu, N. S. H.; Hien, P. V.; Man, T. V.; Thu, V. T. H.; Tri, M. D.; Nam, N. D. A study on corrosion inhibitor for mild steel in ethanol fuel blend. *Materials* **2018**, *11*, 59−70.
(12) Jafari, H.; Idris, M. H.; Ourdjini, A.; Rahimi, H.; Ghobadian, B. Effect of ethanol as gasoline additive on vehicle fuel delivery system corrosion. *Mater. Corros.* **2010**, *61*, 432−440.
(13) Baena, L. M.; Gómez, M.; Calderón, J. A. Aggressiveness of a 20% bioethanol−80% gasoline mixture on autoparts: I behavior of metallic materials and evaluation of their electrochemical properties. *Fuel* **2012**, *95*, 320−328.
(14) Thangavelu, S. K.; Ahmed, A. S.; Ani, F. N. Corrosive characteristics of bioethanol and gasoline blends for metals. *Int. J. Energy Res.* **2016**, *40*, 1704−1711.
(15) Jafari, H.; Idris, M. H.; Ourdjini, A.; Rahimi, H.; Ghobadian, B. EIS study of corrosion behavior of metallic materials in ethanol blended gasoline containing water as a contaminant. *Fuel* **2011**, *90*, 1181−1187.
(16) Groysman, A. *Corrosion in Systems for Storage and Transportation of Petroleum Products and Biofuels: Identification, Monitoring and Solutions*; Springer Science Business Media: Dordrecht, 2014.
(17) Weisburger, J. H. Comments on the history and importance of aromatic and heterocyclic amines in public health. *Mutat. Res., Fundam. Mol. Mech. Mutagen.* **2002**, *506−507*, 9−20.
(18) Abdullah Dar, M. A review: plant extracts and oils as corrosion inhibitors in aggressive media. *Ind. Lubr. Tribol.* **2011**, *63*, 227−233.
(19) Rani, B. E. A.; Basu, B. B. J. Green inhibitors for corrosion protection of metals and alloys: An overview. *Int. J. Corros.* **2012**, *2012*, 1−15.
(20) Mo, S.; Luo, H. Q.; Li, N. B. Plant extracts as "green" corrosion inhibitors for steel in sulphuric acid. *Chem. Pap.* **2016**, *70*, 1131−1143.
(21) Sastri, V. S. *Green Corrosion Inhibitors: Theory and Practice*; John Wiley & Sons: Hoboken, New Jersey, 2011.
(22) Lamaka, S. V.; Zheludkevich, M. L.; Yasakau, K. A.; Montemor, M. F.; Ferreira, M. G. S. High effective organic corrosion inhibitors for 2024 aluminium alloy. *Electrochim. Acta* **2007**, *52*, 7231−7247.
(23) Tan, Y.; Aung, N. N.; Liu, T. Evaluating localised corrosion intensity using the wire beam electrode. *Corros. Sci.* **2012**, *63*, 379−386.
(24) Mohanraj, V. J.; Chen, Y. Nanoparticles − A Review. *Trop. J. Pharm. Res.* **2006**, *5*, 561−573.
(25) Macwan, D. P.; Dave, P. N.; Chaturvedi, S. A review on nano-TiO_2 sol-gel type syntheses and its applications. *J. Mater. Sci.* **2011**, *46*, 3669−3686.
(26) Menard, A.; Drobne, D.; Jemec, A. Ecotoxicity of nanosized TiO_2. Review of in vivo data. *Environ. Pollut.* **2011**, *159*, 677−684.
(27) Lamaka, S. V.; Zheludkevich, M. L.; Yasakau, K. A.; Serra, R.; Poznyak, S. K.; Ferreira, M. G. S. Nanoporous titania interlayer as reservoir of corrosion inhibitors for coatings with self-healing ability. *Prog. Org. Coat.* **2007**, *58*, 127−135.
(28) Hanemann, T.; Szabó, D. V. Polymer-nanoparticle composites: From synthesis to modern applications. *Materials* **2010**, *3*, 3468−3517.
(29) Kango, S.; Kalia, S.; Celli, A.; Njuguna, J.; Habibi, Y.; Kumar, R. Surface modification of inorganic nanoparticles for development of organic−inorganic nanocomposites - A review. *Prog. Polym. Sci.* **2013**, *38*, 1232−1261.
(30) Tompsett, G. A.; Bowmaker, G. A.; Cooney, R. P.; Metson, J. B.; Rodgers, K. A.; Seakins, J. M. The raman spectrum of Brookite, TiO_2 (*Pbca*, Z = 8). *J. Raman Spectrosc.* **1995**, *26*, 57−62.
(31) Hien, P. V.; Vu, N. S. H.; Thu, V. T. H.; Somers, A.; Nam, N. D. Study of yttrium 4-nitrocinnamate to promote surface interactions with AS1020 steel. *Appl. Surf. Sci.* **2017**, *412*, 464−474.
(32) Jones, D. A. *Principles and Prevention of Corrosion*, 2nd ed.; Printice Hall: Upper Saddle River, New Jersey, 1996.
(33) Bahlakeh, G.; Ramezanzadeh, M.; Ramezanzadeh, B. Experimental and theoretical studies of the synergistic inhibition effects between the plant leaves extract (PLE) and zinc salt (ZS) in

DOI: 10.1021/acsomega.8b02084
ACS Omega 2019, 4, 146−158

corrosion control of carbon steel in chloride solution. *J. Mol. Liq.* **2017**, *248*, 854−870.
(34) Ramezanzadeh, M.; Sanaei, Z.; Bahlakeh, G.; Ramezanzadeh, B. Highly effective inhibition of mild steel corrosion in 3.5% NaCl solution by green Nettle leaves extract and synergistic effect of eco-friendly cerium nitrate additive: Experimental, MD simulation and QM investigations. *J. Mol. Liq.* **2018**, *256*, 67−83.
(35) Srivastava, V.; Haque, J.; Verma, C.; Singh, P.; Lgaz, H.; Salghi, R.; Quraishi, M. A. Amino acid based imidazolium zwitterions as novel and green corrosion inhibitors for mild steel: Experimental, DFT and MD studies. *J. Mol. Liq.* **2017**, *244*, 340−352.
(36) Saha, S. K.; Dutta, A.; Ghosh, P.; Sukul, D.; Banerjee, P. Novel Schiff-base molecules as efficient corrosion inhibitors for mild steel surface in 1 M HCl medium: experimental and theoretical approach. *Phys. Chem. Chem. Phys.* **2016**, *18*, 17898−17911.
(37) Mishra, A.; Verma, C.; Lgaz, H.; Srivastava, V.; Quraishi, M. A.; Ebenso, E. E. Synthesis, characterization and corrosion inhibition studies of N-phenyl-benzamides on the acidic corrosion of mild steel: Experimental and computational studies. *J. Mol. Liq.* **2018**, *251*, 317−332.
(38) Dutta, A.; Saha, S. K.; Adhikari, U.; Banerjee, P.; Sukul, D. Effect of substitution on corrosion inhibition properties of 2-(substituted phenyl) benzimidazole derivatives on mild steel in 1 M HCl solution: A combined experimental and theoretical approach. *Corros. Sci.* **2017**, *123*, 256−266.
(39) Dutta, A.; Saha, S. K.; Banerjee, P.; Patra, A. K.; Sukul, D. Evaluating corrosion inhibition property of some Schiff bases for mild steel in 1 M HCl: competitive effect of the heteroatom and stereochemical conformation of the molecule. *RSC Adv.* **2016**, *6*, 74833−74844.
(40) Sastri, V. S.; Perumareddi, J. R. Molecular orbital theoretical studies of some organic corrosion inhibitors. *Corrosion* **1997**, *53*, 617−622.
(41) Kokalj, A. On the HSAB based estimate of charge transfer between adsorbates and metal surfaces. *Chem. Phys.* **2012**, *393*, 1−12.
(42) Obot, I. B.; Macdonald, D. D.; Gasem, Z. M. Density functional theory (DFT) as a powerful tool for designing new organic corrosion inhibitors. Part 1: An overview. *Corros. Sci.* **2015**, *99*, 1−30.
(43) Musa, A. Y.; Jalgham, R. T. T.; Mohamad, A. B. Molecular dynamic and quantum chemical calculations for phthalazine derivatives as corrosion inhibitors of mild steel in 1 M HCl. *Corros. Sci.* **2012**, *56*, 176−183.
(44) Musa, A. Y.; Kadhum, A. A. H.; Mohamad, A. B.; Takriff, M. S. Molecular dynamics and quantum chemical calculation studies on 4,4-dimethyl-3-thiosemicarbazide as corrosion inhibitor in 2.5 M H_2SO_4. *Mater. Chem. Phys.* **2011**, *129*, 660−665.
(45) Ju, H.; Ding, L.; Sun, C.; Chen, J. J. Quantum chemical study on the corrosion inhibition of some oxadiazoles. *Adv. Mater. Sci. Eng.* **2015**, *2015*, 1−5.
(46) ASTM D1193-06. *Standard Specification for Reagent Water*; ASTM International: West Conshohocken, PA, 2018.
(47) ASTM D7577-12. *Standard Test Method for Determining the Accelerated Iron Corrosion Rating of Denatured Fuel Ethanol and Ethanol Fuel Blends*; ASTM International: West Conshohocken, PA, 2012.

DOI: 10.1021/acsomega.8b02084
ACS Omega 2019, 4, 146−158